Experimental and Numerical Investigation of the Precipitation of Barium Sulfate in a Rotating Liquid Film Reactor

Shengchang Guo, David G. Evans, Dianqing Li, and Xue Duan
State Key Laboratory of Chemical Resource Engineering, Beijing University of Chemical Technology, Beijing 100029, P. R. China

DOI 10.1002/aic.11818
Published online June 24, 2009 in Wiley InterScience (www.interscience.wiley.com).

Precipitation of nanosized barium sulfate in a rotating liquid film reactor (RLFR) has been investigated experimentally and through simulations based on the computational fluid dynamics technique including the population balance equation coupled with the Navier–Stokes equations, renormalization group k–ε model equations, and species transport equations. A comparative experiment was carried out involving conventional precipitation in a flask. The structure of the precipitate was identified by powder X-ray diffraction (PXRD), which showed that the crystals obtained using the RLFR were smaller in size than those obtained in the flask. Transmission electron microscopy (TEM) images demonstrated that the crystals produced by the two different processes had different morphologies. Further detailed experiments involving varying the operating parameters of the RLFR were performed to investigate the effects on crystal size distribution (CSD). Increasing the speed of the rotor in the RLFR in the range 1000–5000 rpm or increasing the rotor-stator gap in the range 0.1–0.5 mm resulted in a decrease in particle size and narrower particle size distributions. The simulation results suggested that turbulent effects and reaction processes in the effective reactor space were directly related to rotor speed and rotor-stator gap. The simulated volume weighted mean diameter and CSD of particles of barium sulfate were almost identical to the corresponding experimental results obtained using TEM and laser particle size analyzer. The effects of other parameters such as the Kolmogorov scale and competition between induction time and mixing time are also discussed.
 AIChE J, 55: 2024–2034, 2009
Keywords: precipitation, barium sulfate, rotating liquid film reactor, computational fluid dynamics, population balance, crystal size distribution

Introduction

Precipitation of particles with controlled morphology and crystal size distribution (CSD) is of considerable importance in the chemical industry. The process involves both parallel and consecutive steps: mixing, reaction in the liquid phase, growth, and secondary processes such as agglomeration, aggregation, and disaggregation.[1] The whole process can be very fast and is generally influenced by the relative values of the mixing rate and precipitation rate. The properties of the bulk solid product are strongly dependent on the properties of its constituent particles, such as crystal size, CSD, crystal structure, morphology, and surface area. Great efforts have been made to devise new processes and optimize process parameters to obtain materials with properties tailored for specific requirements, e.g., the formation of nanosized

Correspondence concerning this article should be addressed to D. Li at lidq@mail.buct.edu.cn

particles with a narrow CSD. Experimental investigation and simulation of the dependence of crystal size and CSD on the reactor type and process parameters is thus of key practical importance.

As a consequence of its fast nucleation and crystal growth kinetics, barium sulfate is widely used as a model system to assess the effect of mixing in reactors and to test precipitation models.[2] Precipitation using different types of reactors has been shown to afford materials with a variety of CSD and crystal morphologies. Torbacke and Rasmuson[3] investigated mixing effects in a loop reactor and found that the weight mean size of product increased with increasing macroscale circulation. Baldyga and Pohorecki,[4] Phillips et al.,[5] David,[6] and Bernard-Michel et al.[7] used batch reactors under different conditions and discussed the effect of mixing on various scales (macro-, meso-, and micro-mixing). The influence of varying the turbulent hydrodynamic parameters on the properties of solid particles in a coaxial mixing jet reactor has been studied by Baldyga and Orciuch,[8,9] Falk and Schaer,[10] and Öncül et al.[11] A spinning disk reactor has been used to precipitate small particles of barium sulfate by Cafiero et al.[12] and Couette-type precipitators have been used by Barresi et al.[13] and Judat and Kind[14] to investigate the effect of varying the operating conditions on particle size. However, micrometer-sized particles were obtained in most of the above studies. Recent studies of nanoparticle precipitation in microreactors with a small reaction area have also been reported. For example, a T-mixer reactor with millimeter scale and a membrane reactor with 1.0 mm inner diameter were used by Schwarzer and Peukert[15,16] and Jia et al.,[17] respectively to prepare $BaSO_4$ particles with crystal sizes all on the nanoscale.

The use of computational fluid dynamics (CFD) to predict the performance of chemical processes has risen dramatically in recent years.[18] CFD is a useful tool for simulating relatively complicated systems involving heat transfer, chemical reactions, and multiphase phenomena. To simulate the CSD of the product in a precipitation process, combination of the CFD technique with the population balance model (PBM) is essential. Marchisio and Barresi[19] simulated turbulent precipitation in a semibatch Taylor-Couette reactor using the CFD technique and solved the population balance equation (PBE) using the standard moment method (SMM). Falk and Schaer[10] used a full probability density function (PDF) method coupled with the commercial CFD package Fluent for flow field prediction and CSD simulation. Accurate calculations of the PBE are based on the discretization method, which requires large calculation times and gives rise to many memory problems. Discretization methods have been developed by Kumar and Ramakrishna[20] for aggregation and breakage, and by Marchal et al.[21] and Muhr et al.[22] for aggregation and crystal growth. A reasonably simple and accurate alternative method, the quadrature method of moments, was used by Marchisio et al.[23] to solve the PBE when simulating precipitation using CFD.

A colloid mill is a grinding device, which is designed for breaking up large wet particles in the food, pharmaceutical, and chemical industry.[24] It can promote the efficient grinding of solid particles and intensify the mass transfer, heat transfer, and momentum transfer as well as reaction processing by means of the high shear forces generated by the rotor-stator system. We have recently shown that a suitably modified colloid mill can also be used as a reactor to prepare new functional nanoparticles and that, compared with conventional precipitation processes in a stirred tank, the colloid mill reactor gives materials with smaller crystal size and narrower CSD. A series of functional materials[25–27] and their derivatives such as flame retardants,[28] PVC thermal stabilizers,[29] and selective IR absorption materials[30] have been prepared using the colloid mill reactor. A commercial colloid mill cannot be directly used as a reactor to produce nanosized functional materials because there are disadvantages such as lack of reproducibility caused by the influence of air drawn into the reactor along with the reactants. To overcome these factors, the inlet of the colloid mill reactor was modified as described below. We refer here to the modified colloid mill reactor as a rotating liquid film reactor (RLFR).

The mechanism of mixing and the influence of varying the experimental parameters on the precipitation process in an RLFR have not previously been studied. Experimental and theoretical simulations are indispensable to gain a deeper understanding of the RLFR and to be able to tailor the mixing properties to produce materials with the desired properties. In this work, precipitation of barium sulfate is used as a model reaction system to investigate the fast mixing properties and complex reaction steps occurring in an RLFR. The aim is to precipitate nanosized barium sulfate with narrow CSD in the RLFR and show the impact of varying the operating parameters on the CSD, as an example of product properties, by a combination of experimental and numerical methods.

Experimental

Precipitation reactor

The key component of the RLFR consists of a rotor-stator system as shown in Figure 1. The inlet above the rotor originally consisted of four blades (shown crosshatched in Figure 1). This was modified by conversion to a solid column with two solution inlet pipes to minimize the intake of air along with the solutions. The rotor is frustum-like, with a height of 17 mm, upper diameter of 40.8 mm, and bottom diameter of 50 mm. It can rotate at variable speeds up to 5000 rpm by adjustment of a 1 kW variable-speed motor. The angle between the bottom plane and the side edge is 75° as shown in the expanded view in Figure 1a. The gap h between rotor and stator can be adjusted in the range 0.1–0.5 mm by moving the stator.

Experimental procedures

$BaCl_2$ (317 g; 99% purity) and 218 g Na_2SO_4 (99% purity) were separately dissolved in distilled water to make 1 L of 1.3 M $BaCl_2$ solution and 1 L of 1.3 M Na_2SO_4 solution, the latter being a saturated solution. The two solutions were simultaneously fed into the RLFR through two separate feed pipes by a peristaltic pump (ZT60-600a) with a given rotor speed, rotor-stator gap, and addition rate of solution. Temperature was maintained at 25°C by a jacket connected to a circulating water system. The resulting slurry was then centrifuged and washed to remove Cl^- and Na^+ ions to reduce the agglomeration effect. The cake was dried at 70°C for 24 h.

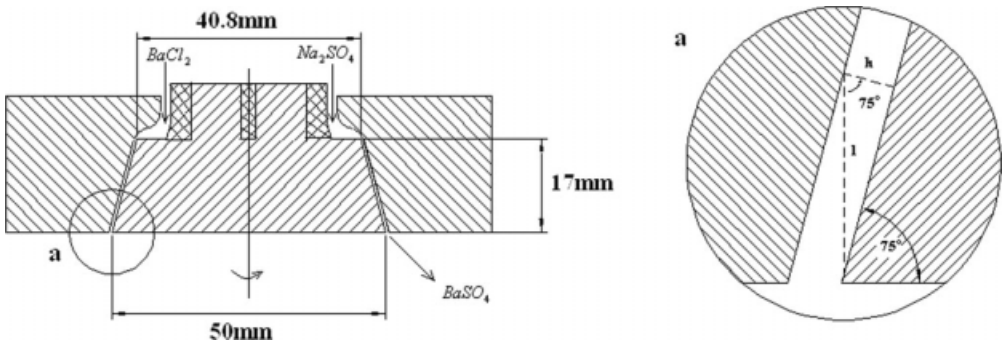

Figure 1. Sketch diagrams of the RLFR.

To compare the CSD of barium sulfate prepared by the RLFR and a conventional reactor, precipitation of barium sulfate was carried out in a flask with stirring of the mixture at 100 rpm.

Characterization

Powder X-ray diffraction patterns were recorded on a Shimadzu PXRD-6000 diffractometer (Cu Kα radiation, scan speed of 5° per min). For each sample, the crystal size and morphology was characterized using a Hitachi H-800 transmission electron microscope (TEM) by counting the primary particles in three images. Every CSD was measured with a Mastersizer 2000 laser particle size analyzer employing the Mie model. The refractive index of barium sulfate is 1.637.

Reaction Kinetics and Model Equations

Precipitation is a phase transformation process. To investigate the effect of the RLFR on precipitation, it is necessary to simulate the PBM, including both nucleation and growth rates as a function of supersaturation.

Reaction kinetics

Supersaturation. The thermodynamic driving force for precipitation is created by the mixing of the $BaCl_2$ and Na_2SO_4 solutions. Because the solubility of the precipitated product is low, the supersaturation is usually high. Ion activities instead of concentrations are used for the calculation of the supersaturation. The method described by Vicum et al.[31] was used in this work.

Barium sulfate precipitates from aqueous solutions of barium chloride and sodium sulfate according to the chemical equation below

$$BaCl_2 + Na_2SO_4 \rightarrow BaSO_4 \downarrow + 2NaCl \tag{1}$$

The supersaturation S based on activities is defined as follows

$$S = \gamma \sqrt{\frac{C_{Ba^{2+}} C_{SO_4^{2-}}}{K_{sp}}} \tag{2}$$

where the value of thermodynamic solubility product $K_{sp} = 1.08 \times 10^{-10}$ mol^2 L^{-2} at 25°C, and the activity coefficient $\gamma = 0.07$.

Nucleation. After the creation of a driving force for precipitation, collisions of solute molecules take place with varying efficiencies resulting in the formation of clusters, which subsequently become a nucleus with a critical number of molecules n^* when the energy barrier to the homogenous formation of the critical nucleus, ΔG_{hom}, is overcome.

According to the Gibbs-Thomson relation, the energy ΔG_{hom} and critical number n^* can be derived as follows[12]

$$\Delta G_{hom} = \beta v_0^2 \gamma^{s3} / \varphi^2, \tag{3}$$

$$n^* = \Delta G_{hom} / \varphi, \tag{4}$$

where β is a geometric factor taken as 116, the appropriate value for particles that are essentially spherical in shape; v_0 represents the molecular volume; γ^s is the surface energy, which is equal to 0.136 J m^{-2}; φ denotes the reaction affinity and is equal to 7.76×10^{-20} J.

The resultant number of molecules is ~4.6 and can be assumed to be an integer, 5, which means that the nucleation will start if a cluster is made up of more than five molecules. Considering that the molecular diameter of $BaSO_4$ is 0.44 nm, the last critical nucleus size is 1.1 nm, which was set as the initial particle size in the PBM.

The nucleation rate of forming a critical size nucleus can be represented, according to the classical primary nucleation theory by[11]

$$B = B^0 \exp\left(-\frac{A}{\ln^2 S}\right) \tag{5}$$

where $B^0 = 1 \times 10^{36}$ number of crystals·(m^3 s)$^{-1}$ and $A = 2686$ for $S \geq 1000$ and $B^0 = 1.46 \times 10^{-12}$ number of crystals·(m^3 s)$^{-1}$ and $A = 67.3$ for $1 < S < 1000$.

Crystal growth. The crystal growth process is generally explained as the integration of atoms into the crystal lattice. The overall growth rate G as a function of supersaturation is expressed by the relation[32]

$$G = k_g (S-1)^2 \tag{6}$$

where k_g is the growth rate constant and is equal to 4×10^{-11} m s^{-1}.

Aggregation. Aggregation in precipitation can be considered as a secondary process because it not only occurs during solid formation through reduction of supersaturation but

also afterwards.[16] Aggregates of primary particles can be held together by forces such as van der Waals forces, dipole–dipole forces, and hydrogen bonding.

A particle of size L is formed (born) when particles of sizes L_i and L_j aggregate, leading to the concept of birth rate, B_{agg}. Conversely, particles L_i and L_j can vanish (die), leading to the concept of death rate, D_{agg}, where

$$B_{agg}(n,L) = \frac{L^2}{2}\int_0^{\infty} \frac{\beta_{agg}(\sqrt[3]{L^3-l^3}, l)n(\sqrt[3]{L^3-l^3})n(l)}{(L^3-l^3)^{2/3}}dl \quad (7)$$

$$D_{agg}(n,l) = n(L)\int_0^{\infty} \beta_{agg}(L,l)n(l)dl \quad (8)$$

Here $n(L)$ and $n(l)$ are the number density concentrations of particles of size L and l, respectively, and $\beta_{agg}(x,y)$ represents the aggregation rate kernel. For shearing force domain interactions of fluid and particles in the flow field, we take the kernel in the shear flow with length coordinate as[33]

$$\beta_{agg}(x,y) = G_s K_a (x+y)^3 \quad (9)$$

where the constant K_a has the meaning of a coalescence rate constant, and its value for laminar flow is taken as 4/3, whereas that for turbulent flow is 1.294, G_s is the shear rate that is related to local value of turbulent energy dissipation rate ε and the kinematic viscosity v_L as

$$G_s = (\varepsilon/v_L)^{1/2} \quad (10)$$

where v_L is kinematic viscosity of the solution.

CFD and PBM

Theoretical simulation by CFD techniques coupled with PBM was used to model precipitation in the RLFR. The standard set of the Reynolds-averaged Navier–Stokes equations, and the continuity equation as well as the two equations of renormalization group (RNG) k–ε model were applied to simulate the flow field. All the necessary equations for fluid simulation are available in the commercial software Fluent.

The status of the flow is represented as the Reynolds number, which is defined as

$$R_e = \omega L_1 (L_2 - L_1)/v_L \quad (11)$$

where ω is the angle speed of the inner rotor, and L_1 and L_2 is the mean radius of the stator and rotor, respectively. The flows become turbulent at large Reynolds number. Although there is no unique Reynolds number indicating the onset of turbulent flow; however, the results show that once the Reynolds number is of the order of 2000 or more, transition to turbulent flow generally occurs. For the RLFR, the Reynolds number is in the range 680–3487 over the operating conditions used. There will be turbulent flows if the rotor speed exceeds 3000 rpm for a rotor-stator gap >0.3 mm. Thus, we used the laminar model at low rotor speeds and small rotor-stator gaps, whereas the RNG k–ε model was used at high rotor speeds and large rotor-stator gaps.

The equation for species transport in the reaction process that we used was described by Öncül et al.[11]

$$\frac{\partial \rho(C_i)}{\partial t} + \nabla \cdot (\rho u C_i - \Gamma_{eff} \nabla C_i) = S_{Ci} \quad (12)$$

where C_i represent the concentrations of Ba^{2+}, Cl^-, Na^+, SO_4^{2-}, and $BaSO_4$. The source term for the nonreacting ions of S_{Ci} (Cl^-, Na^+) was set to zero, while for the other three species its magnitude was set as the specific crystal growth rate S_g with positive sign for $BaSO_4$ and negative sign for Ba^{2+} and Cl^-. The effective turbulent diffusivity, Γ_{eff}, was computed as

$$\Gamma_{eff} = \frac{C_\mu k^2}{S_c \varepsilon} \quad (13)$$

where k is turbulent kinetic energy, ε is rate of kinetic energy dissipation, Schmidt number $S_c = 0.7$, $C_\mu = 0.09$.

The specific crystal growth rate is related to the second moment of the CSD, m_2, as shown

$$S_g = (3m_2 G)K_v \frac{\rho_{BaSO_4}}{M_{BaSO_4}} \quad (14)$$

where the volumetric crystal shape factor $K_v = \pi/6$.

For precipitation in the RLFR, there are no crystal seeds in the feed point, and the system is in a steady state with constant volume. The final CSD was evaluated from the PBM as proposed by Randolph and Larson[34]

$$\frac{\partial n}{\partial t} + \nabla(un) + \frac{\partial Gn}{\partial L} = \nabla(\Gamma_{eff}\nabla n) + B - D \quad (15)$$

where n is the number density function, and L is the crystal size.

To solve the PBE, the SMM approach was applied. The jth moments are defined as

$$m_j = \int_0^{\infty} L^j n dL \quad (j = 0-4). \quad (16)$$

The first five moments ($j = 0$, 1, 2, 3, and 4) are of particular interest, because they are related to the total number particle density, the total particle area, and the total solids volume. Equation 15 can be transformed to a series of equations using first five moments as follows

$$\frac{\partial m_j}{\partial t} + \nabla(\vec{u} m_j) = \nabla(\Gamma_{eff}\nabla m_j) + 0^j B^0 + jGm_{j-1} + \overline{B}_j - \overline{D}_j \quad (j = 0-4) \quad (17)$$

where

$$\overline{B}_j = \int_0^{\infty} L^j B dL, \quad (18)$$

$$\overline{D}_j = \int_0^{\infty} L^j D dL. \quad (19)$$

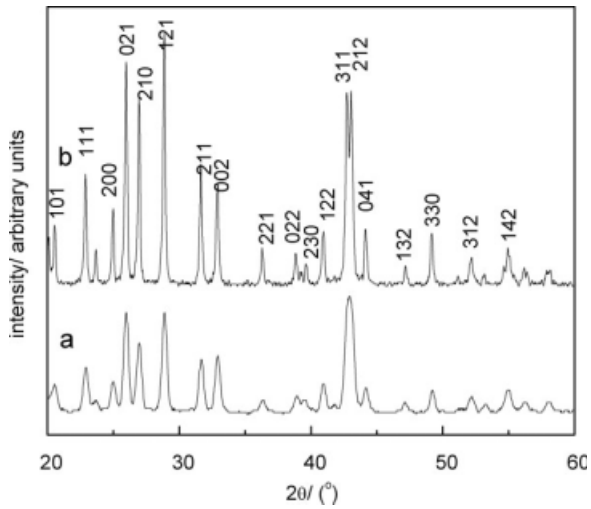

Figure 2. PXRD patterns of $BaSO_4$ prepared in the RLFR (a) and flask (b).

The resulting volume weighted mean diameter (VWMD) is defined as the ratio of the fourth moment to the third moment

$$d_{43} = \frac{m_4}{m_3} \tag{20}$$

and the solid concentration is defined as

$$C_{BaSO_4} = m_3 K_v \frac{\rho_{BaSO_4}}{M_{BaSO_4}}. \tag{21}$$

To characterize the CSD from the calculated moments, two additional quantities of mean size ($\bar{x}$) and coefficient variation (c_v) should be computed as[35]

$$\bar{x} = \frac{m_1}{m_0}, \tag{22}$$

$$c_v = \sqrt{\frac{m_0 m_2}{m_1^2} - 1}\ . \tag{23}$$

The log–normal function with two parameters was used to reconstruct the CSD

$$f(x) = \frac{1}{x \ln\sigma_g \sqrt{2\pi}} \exp\left(-\frac{\ln^2(x/\bar{x}_g)}{2\ln^2\sigma_g}\right) \tag{24}$$

where

$$\bar{x}_g = \frac{\bar{x}}{\exp(0.5\ln^2\sigma_g)}, \tag{25}$$

$$\sigma_g = \exp\left(\sqrt{\ln(c_v^2 + 1)}\right). \tag{26}$$

Experimental Results

Crystal structure and morphology

The powder X-ray diffraction patterns (PXRD) of barium sulfate precipitated in the RLFR (a) and flask (b) are shown in Figure 2. All the peaks can be indexed to the characteristic pattern of barium sulfate with unit cell constants a = 7.144 Å, b = 8.865 Å, and c = 5.445 Å, which agree well with the standard value (JCPDS no. 24-1035). The PXRD pattern of barium sulfate precipitated in the flask has considerably narrower and stronger diffraction peaks. In contrast, however, the PXRD pattern of barium sulfate precipitated in the RLFR consists of weak peaks with a large full width at half-maximum (FWHM). The (311) and (212) reflections have been merged, which suggest that the growth of specific crystal faces was altered. Crystal size can be estimated according to the empirical Scherrer equation[36]

$$L = \frac{0.89\lambda}{\beta(\theta)\cos\theta} \tag{27}$$

where L is the crystallite size, λ is the wavelength of the radiation used, θ is the Bragg diffraction angle, and $\beta(\theta)$ is the FWHM.

The crystal size of the precipitate formed in the RLFR is 18.2 nm, whereas that of the precipitate formed in the flask is 43.7 nm as calculated from the PXRD data as shown in Figure 2.

Figure 3 shows the TEM images of the crystal morphologies of barium sulfate precipitated in the RLFR (a) and in the flask (b). As shown in Figure 3a, the VWMD of particles

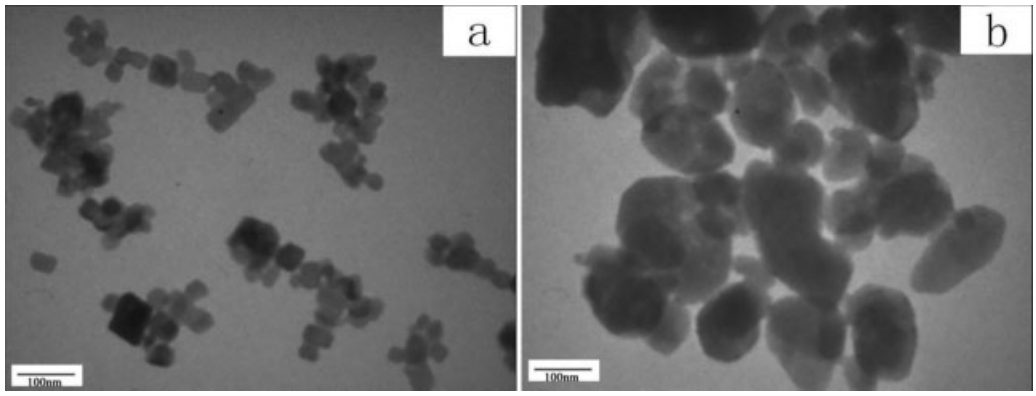

Figure 3. TEM images of $BaSO_4$ prepared in the RLFR (a) and flask (b).

Table 1. Critical Volume Flow Rates of Each Pair of Rotor Speed and Rotor-Stator Gap

Rotor Speed (rpm)	Critical Volume Flow Rate (mL min^{-1})				
	0.1 mm	0.2 mm	0.3 mm	0.4 mm	0.5 mm
1000	6	8	20	40	75
2000	11	32	47	85	150
3000	36	55	85	152	218
4000	51	71	140	250	324
5000	66	85	200	380	420

prepared using the RLFR was 45 nm, and they had uniform crystal size. The crystal morphology was cubic-like and clear boundaries between crystals were observed. In contrast, the crystals precipitated in the flask (Figure 3b) have a larger VWMD of 150 nm with a wider CSD and much more irregular crystal morphology. The reason for the differences in the crystal sizes calculated by PXRD and TEM is probably due to the Scherrer equation being an empirical equation with a relatively large error.

The PXRD patterns and TEM images both suggest that the RLFR has a significant effect on the nucleation and growth habit of barium sulfate.

Critical volume flow rate

Every combination of rotor speed and rotor-stator gap in the RLFR has a corresponding maximum amount of fluid that can be treated. It should be noted that only liquid and solid phases existed in the reaction system because introduction of air was prevented. The maximum amount of fluid that can be treated is defined as the critical volume flow rate in this work. Table 1 shows the measured critical volume flow rates for pairs of rotor speed and rotor-stator gap. It can be seen that the critical volume flow rate increases rapidly with increasing rotor speed and rotor-stator gap. To avoid any air bubbles entering the RLFR and ensure the maximum amount of fluid was treated, all experiments were carried out at the critical volume flow rate.

Effect of varying rotor speed

Figure 4 shows the effect of varying the rotor speed of the RLFR on the CSD of barium sulfate. Precipitation of barium sulfate was carried out at 1000, 2000, 3000, 4000, and 5000 rpm with the rotor-stator gap fixed at 0.3 mm. As shown in Figure 4, the CSD were strongly affected by the rotor speed with the particle size decreasing and CSD becoming narrower with increasing rotor speed. This is quite different from the behavior observed in a stirred tank where either a maximum[37,38] or a minimum[39] with an inflection has been previously observed, suggesting that the mechanism of precipitation of barium sulfate in the RLFR was different from that in a stirred tank.

The effect of varying the rotor speed in the RLFR on the CSD can be attributed to the result of interactions between mixing, crystal nucleation, and growth kinetics. CSD is determined by the competition between nucleation and growth; both of these depend on supersaturation with strongly nonlinear functions as shown in Eqs. 5 and 6. Any decrease in supersaturation will lead to decrease in nucleation rate, which reduces the number of particles that can precipitate and therefore increases the consumption of supersaturation by crystal growth. This results in larger crystal size and wider CSD of the product. For these reasons, the short mixing time and uniform instantaneous supersaturation obtained at high rotor speed lead to small VWMD and narrow CSD in the product synthesized in the RLFR.

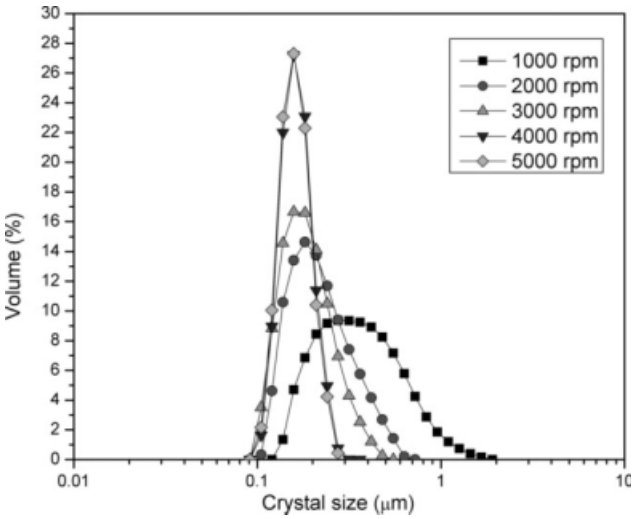

Figure 4. The effect of varying rotor speed on CSD of barium sulfate with a rotor-stator gap of 0.3 mm at the critical volume flow rate.

Effect of varying rotor-stator gap

Rotor-stator gaps of 0.1, 0.2, 0.3, 0.4, and 0.5 mm were examined with a fixed rotor speed. The CSD of the products of each experiment are shown in Figure 5. The CSD decreased with increasing rotor-stator gap, with the variation being most marked in the range 0.1–0.3 mm. This can be explained as follows. In the case of very narrow rotor-stator

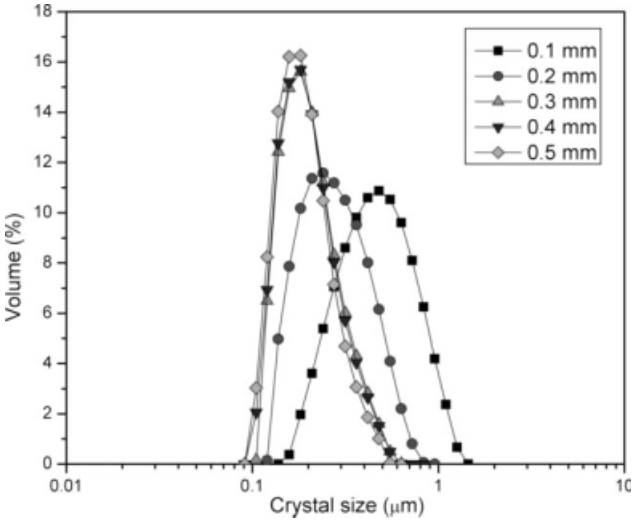

Figure 5. The effect of varying rotor-stator gap on CSD of barium sulfate with a rotor speed of 3000 rpm at the critical volume flow rate.

Table 2. Values of Constants and Properties of Species Used in the Simulations

β	116
B^0	1×10^{36} number of crystals·$(m^3 s)^{-1}$
A	2686
C_μ	0.09
k_g	4×10^{-11} m s^{-1}
K_a	4/3 or 1.294
K_v	$\pi/6$
ρ_{BaSO_4}	4500 kg m^{-3}
ρ_{Na_2SO4}	1162 kg m^{-3}
ρ_{BaCl_2}	1112 kg m^{-3}
ρ_{NaCl}	1080 kg m^{-3}
v_{Na_2SO4}	0.001571 kg $(ms)^{-1}$
v_{BaCl_2}	0.001003 kg $(ms)^{-1}$
v_{NaCl}	0.001112 kg $(ms)^{-1}$

gaps (0.1–0.2 mm), the species transfer process in the narrow rotor-stator gap is dominated by the viscosity effect, and the mixing rate is insufficient and becomes the controlling step of the whole reaction process. This depresses the nucleation rate and gives fewer nuclei. Because more supersaturation is consumed by crystal growth rather than nucleation, the CSD obtained with very narrow rotor-stator gaps have a wide distribution as shown in Figure 5.

Modeling Results

Determination of modeling conditions

In this work, the main equations were solved using the software Fluent (version 6.2) with three-dimensional (3D) simulations in a quarter of the reactor. A hexahedral grid was used in the simulations and the final grid contained 200,000 cells, 585,000 faces, and 215,271 nodes. Nucleation rate and crystal growth rate as well as aggregation rates were added to Fluent as external supplementary user-defined scalar descriptions and solved by user-defined function files developed in this work. The flow field was simulated by standard set of the Reynolds-averaged Navier–Stokes equations accompanied by the continuity with a laminar model at low rotor speeds and small rotor-stator gaps, whereas RNG k-ε model was used for high rotor speeds and large rotor-stator gaps. The species transport equation was simulated by a finite-rate/eddy-dissipation model. The VWMD and CSD were simulated through PBE using SMM and log–normal distribution. The underrelaxation factors associated with the equations were adjusted in a stepwise increasing manner during the simulations because of the extremely stiff numerical character of the rapid reaction speed and crystal growth. It was assumed that convergence was achieved when the sum of normalized residuals was well below 10^{-4}; the solution was kept unchanged for the rest of the simulations. The numerical values of the constants and properties of species are listed in Table 2.

Flow field in the RLFR

The modeling process was considered only for a quarter of the reactor using periodic boundary conditions to reduce the calculation time. As can be seen from Figure 6, the magnitude of the velocity increased along the stator to rotor direction and the inlet to outlet direction for operating conditions of rotor speed of 3000 rpm and rotor-stator gap of 0.3 mm with the critical volume flow rate. To observe the effects of varying the rotor speed and rotor-stator gap on the flow field, we simulated the flow field using the above experimental operating conditions. Figures 7 and 8 show the impact of varying the rotor speed and rotor-stator gap on the magnitude of the velocity along the center line, which is defined as the line connecting the midpoint of the inlet to the midpoint of the outlet of a given section. The x axis corresponds to the position of the center line, on which the value of 0.017 denotes the inlet and 0 denotes the outlet. It

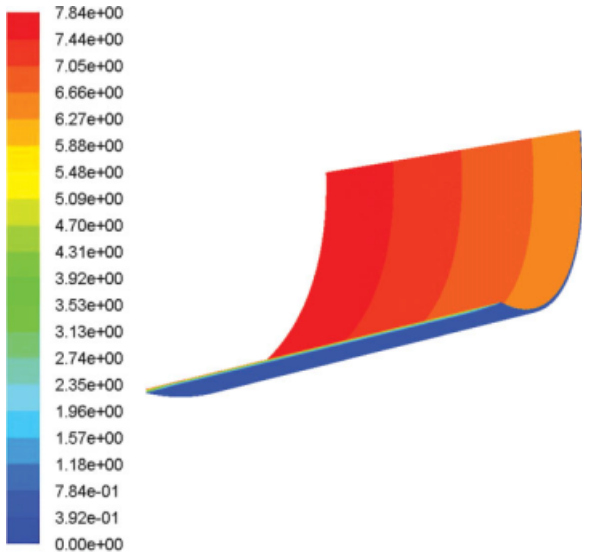

Figure 6. Flow field in the RLFR for rotor speed of 3000 rpm and rotor-stator gap of 0.3 mm at the critical volume flow rate.

[Color figure can be viewed in the online issue, which is available at www.interscience.wiley.com.]

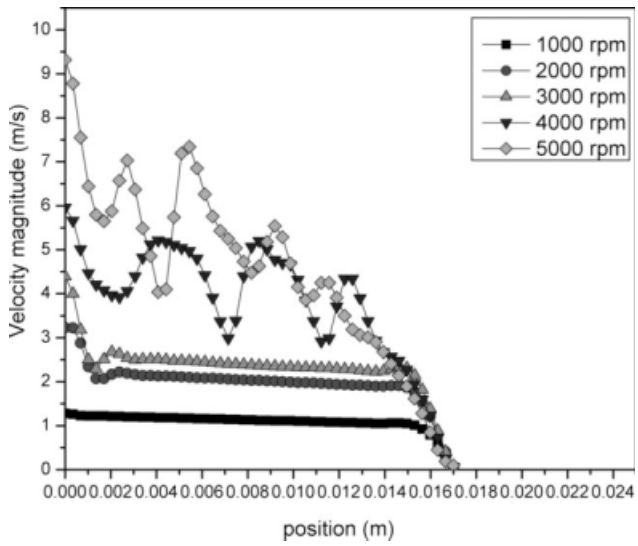

Figure 7. Velocity magnitude on the center line of the RLFR for different rotor speeds with rotor-stator gap of 0.3 mm at the critical volume flow rate.

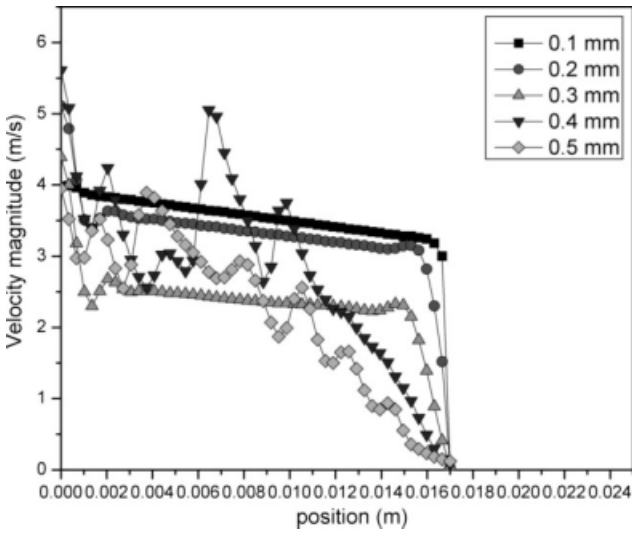

Figure 8. Velocity magnitude on the center line of the RLFR for different rotor-stator gaps with rotor speed of 3000 rpm at the critical volume flow rate.

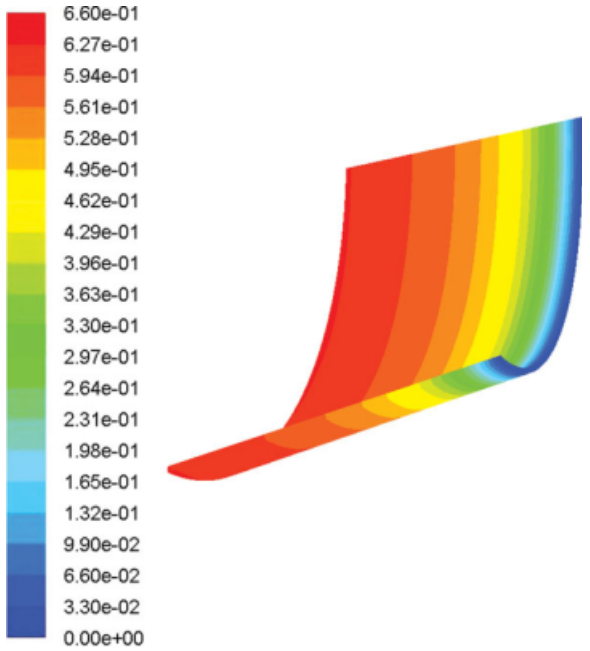

Figure 9. Mass fraction distribution of $BaSO_4$ in the RLFR for a rotor speed of 3000 rpm and rotor-stator gap of 0.3 mm at the critical volume flow rate.

[Color figure can be viewed in the online issue, which is available at www.interscience.wiley.com.]

was found that velocity magnitude increased with increasing rotor speed. The flow field developed oscillations when the rotor speed exceeded 4000 rpm, or the gap is >0.4 mm, which is probably due to the tendency to form Taylor vortices. Full Taylor vortices are hard to be developed because of the restricted space in such narrow gaps. The oscillations will be more severe for higher rotor speed and wider shearing gap. Increasing the rotor speed or rotor–stator gap favors the evolution of Taylor vortices and enhances mixing effects. Thus, it should be easy to produce small crystals at high rotor speeds and wide rotor-stator gaps, which is consistent with the experimental results.

Species transport in RLFR

Figure 9 shows the mass fraction distribution of $BaSO_4$ in a quarter of the RLFR for a rotor speed of 3000 rpm and rotor-stator gap of 0.3 mm with the critical flow rate. The mass fraction of $BaSO_4$ was zero at the inlet of the reactor and increased as the reaction proceeded. Finally, it reached its maximum value of 0.66 (without considering water) at the outlet. The reaction was complete in the reactor, which ensured a homogenous nucleation process and led to the occurrence of small and uniform particles. Figures 10 and 11 show the mass fraction of $BaSO_4$ on the center line for different rotor speeds and rotor-stator gaps respectively. These parameters have similar effects on the mass fraction. At low rotor speeds and narrow rotor-stator gaps, the reaction was incomplete. This indicates that the mixing in the reactor was poor, and this inhibits the reaction process. Varying the rotor-stator gap has a more marked effect than varying the rotor speed.

VWMD and CSD in RLFR

A comparison of CSD (as volume distribution) as measured by TEM and a laser particle size analyzer with the simulated results for the precipitation of $BaSO_4$ with rotor speed of 3000 rpm and rotor-stator gap of 0.3 mm in the RLFR is shown in Figure 12. The difference in the experimental values obtained by TEM and laser particle size analyzer is due to the aggregation of primary particles, as shown in Figure 3. We considered this effect during the simulation to obtain more realistic simulated results. As a comparison, simulation without aggregation effects is also shown in

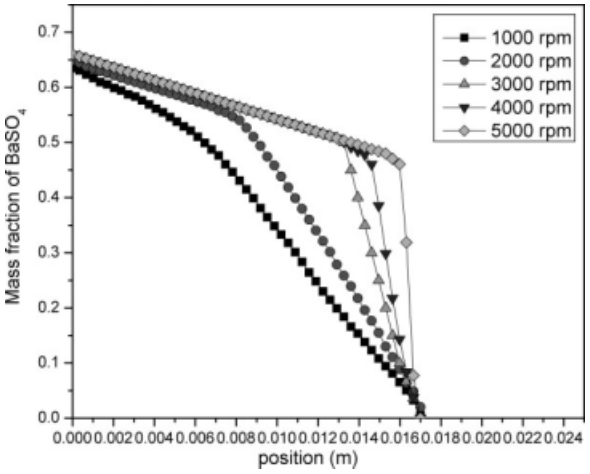

Figure 10. Mass fraction of $BaSO_4$ on the center line of the RLFR for different rotor speeds with rotor-stator gap of 0.3 mm at the critical volume flow rate.

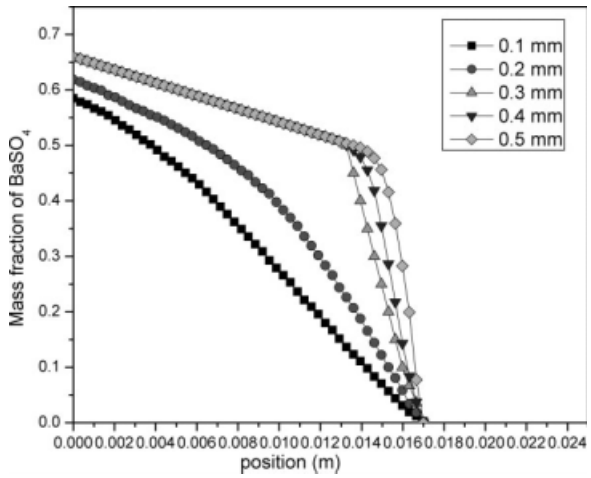

Figure 11. Mass fraction of $BaSO_4$ on the center line of the RLFR for different rotor-stator gaps with rotor speed of 3000 rpm at the critical volume flow rate.

Figure 12. The simulated results are approximately the same as the corresponding experimental results, which suggest that the models and the specific boundary conditions we used are valid for the RLFR and indirectly show that the simulated flow field and mass fraction of $BaSO_4$ in RLFR are correct. Further simulations were carried out to test the applicability of the model for other operating conditions as shown in Figures 13 and 14. The simulated effects of varying the rotor speed and rotor-stator gap on VWMD are the same as that observed experimentally. All the curves showed a decrease in particle size with increasing rotor speed and rotor-stator gap. Generally, the simulated values with, and without, aggregation effects lie above and near the experimental results of laser scattering analysis and TEM, respectively, showing that the simulations are acceptable over the entire range of operating conditions used.

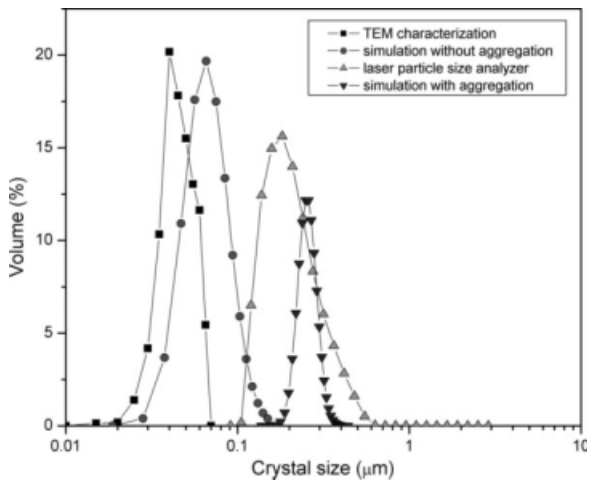

Figure 12. Comparison of CSD of $BaSO_4$ obtained from experiment and simulation at a rotor speed of 3000 rpm and rotor-stator gap of 0.3 mm.

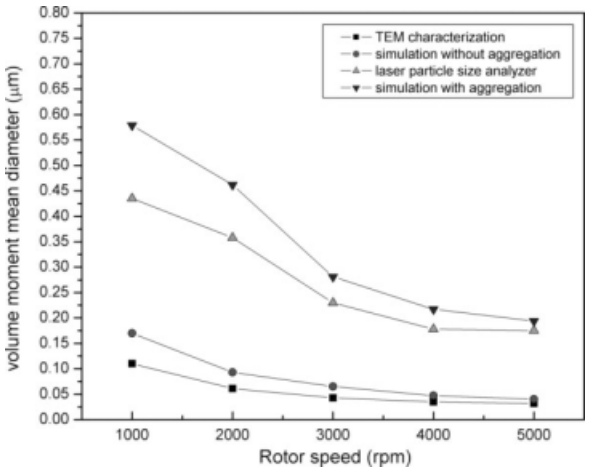

Figure 13. Mean particle size obtained by experiments and simulations for different rotor speeds with rotor-stator gap of 0.3 mm at the critical volume flow rate.

Discussion of the mechanism of precipitation in RLFR

Kolmogorov Scale. The Kolmogorov scale η_k is the smallest length scale of turbulence and is expressed as a function of kinematic viscosity and dissipation rate and is given by

$$\eta_k = \left(\frac{\nu_L^3}{\varepsilon}\right)^{1/4}, \tag{28}$$

$$\varepsilon = \omega^3 L_1^5 / V_R, \tag{29}$$

where V_R is the volume of the reactor.

The Kolmogorov scale η_k is usually in the range 10–100 μm in a stirred tank,[40] whereas in the case of the RLFR, it is only in the range of 1–8 μm, as shown in Figure 15. Such a small Kolmogorov scale can allow the two solutions to

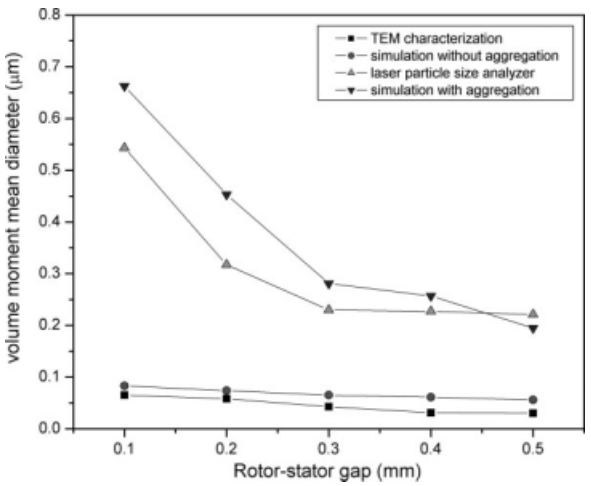

Figure 14. Mean particle size obtained by experiments and simulations for different rotor-stator gaps with rotor speed of 3000 rpm at the critical volume flow rate.

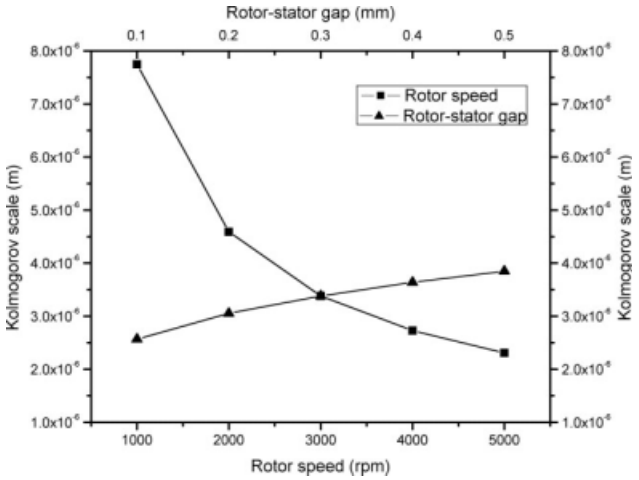

Figure 15. Kolmogorov scale for different combinations of rotor speed and rotor-stator gap.

mix on a molecular scale in a short time and result in particles with a narrow CSD.

Mixing Time and Induction Time. The mixing time t_m is the time elapsed between the initial contact between the two solutions and reaching micromixing on a molecular level. The induction time t_{ind} is defined as the overall time required for the nucleation and growth of the generated crystals to a detectable size. As discussed previously, the CSD is affected by a competition between mixing and reaction kinetics. When t_m is shorter than t_{ind}, the reaction process is the controlling step and the supersaturation has a short-elapsed time resulting in a small particle size with a sharp CSD. In contrast, when the mixing process is the controlling step the resultant particles have larger sizes with a wider CSD.

The induction time t_{ind} and the mixing time t_m were calculated by the equations

$$Log(t_{ind}) = 15.5Log^{-2}S - 4.2, \tag{30}$$

$$t_m = \left(\frac{\nu_L}{\varepsilon}\right)^{1/2}\ln(S_c), \tag{31}$$

where the Schmidt number S_c was taken[12] as 108.59.

For the conditions we adopted in the experiments, the final induction time t_{ind} is 0.3 ms. For high rotor speeds and large rotor-stator gaps, the mixing times are less than the value of t_{ind}, which ensures the sufficient mixing of reactant species before the reaction start. For instance, the calculated value of t_m is 0.1 ms for a rotor speed of 3000 rpm for a rotor-stator gap of 0.3 mm. In contrast, for a rotor speed of 1000 rpm with the same rotor-stator gap the calculated value of t_m is 0.8 ms, larger than t_{ind}.

Summary and Conclusions

Nanosized barium sulfate was precipitated in a new type of reactor, the RLFR, and the product compared with that obtained using a conventional flask reactor. The products precipitated in the RLFR had small crystal size of ~45 nm with narrow CSD as characterized by PXRD and TEM. The effects of varying the operating conditions on CSD were also investigated. The CSD became narrower and VWMD shifted from 0.5 to 0.1 μm with increasing rotor speed and rotor-stator gap. These effects were quite different from precipitation in a stirred tank as reported by other authors, suggesting precipitation in the RLFR has unique mixing and reaction mechanisms.

The flow field and species mass distribution as well as VWMD and CSD of barium sulfate were simulated for the RLFR. The simulated flow field results showed that the turbulent effect increased with increasing rotor speed and rotor-stator gap. The calculated mass distribution of $BaSO_4$ in the RLFR suggested that the reaction was not completed at low rotor speeds and narrow rotor-stator gaps, leading to the observed large particle size. Although the flow field and mass distribution of $BaSO_4$ cannot be investigated directly for such a narrow gap, the good agreement between the values of VWMD and CSD obtained by laser particle size analyzer experiments and simulations including the aggregation model showed that the simulated results of flow field and mass distribution of $BaSO_4$ were acceptable and the models we used were suitable for predicting the CSD of materials prepared in the RLFR. The small Kolmogorov scale below 8 μm and short mixing times <0.3 ms at high rotor speeds in RLFR ensured the occurrence of homogenous nucleation and inhibited the growth of particles, resulting in the formation of nanosized crystals with a narrow CSD.

Acknowledgements

This work was supported by National Natural Science Foundation, 111 Project and Program for Changjiang Scholars and Innovative Research Team in University.

Notation

A = nucleation constant
B = nucleation rate, number of crystal,$\cdot(m^3\ s)^{-1}$
B^0 = initial nucleation rate, number of crystal,$\cdot(m^3\ s)^{-1}$
B_{agg} = birth rate of aggregation, $m^{-4}\ s^{-1}$
C_i = species concentration, kmol $(m^3)^{-1}$ (M)
c_v = coefficient variation
C_μ = constant
d_{43} = volume weighted mean diameter, μm
G = linear growth rate, m s^{-1}
G_s = shear rate, s^{-1}
h = rotor-stator gap of RLFR, mm
k = turbulent kinetic energy, $m^2\ s^{-2}$
K_a = coalescence rate constant
k_g = growth rate constant, m s^{-1}
K_{sp} = thermodynamic solubility product, $mol^2\cdot(L^6)^{-1}$
K_v = shape factor
L = crystal size, m
L_1 = mean diameter of the rotor, m
L_2 = mean diameter of the stator, m
l = crystal size, m
m_j = jth moment, $m^j\ (m^3)^{-1}$
n = number density concentration of particles, m^{-4}
n^* = critical number of molecules
S = supersaturation
S_c = Schmidt number
S_{Ci} = chemical species source term, kg kmol $(m^6 s)^{-1}$
S_g = specific crystal growth, kmol $(m^3 s)$
t = time, s
t_{ind} = induction time, s
t_m = mixing time, s
V_R = volume of the RLFR, m^3
$\bar{x}$ = mean size
$\bar{x}_g$ = mean of log–normal distribution

Greek letters

β = geometric factor
β_{agg} = aggregation rate constant, i.e., aggregation kernel, $m^3\ s^{-1}$
$\beta(\theta)$ = peak width at half-height
γ = activity coefficient
η = shear stress, $N\ m^{-2}$
Γ_{eff} = effective diffusivity, $kg\ (ms)^{-1}$
γ^s = surface energy, $J\ (m^2)^{-1}$
ΔG_{hom} = Gibbs energy change of homogeneous nucleation, J
ε = turbulent energy dissipation rate, $m^2\ s^{-3}$
η_k = Kolmogorov scale, μm
θ = Bragg diffraction angle
λ = wavelength of the radiation
ν = kinetic viscosity, $kg\ (ms)^{-1}$
ν_L = kinematic viscosity, $m^2\ s^{-1}$
ν_0 = molecular volume, m^3
ρ = density, $kg\ m^{-3}$
σ_g = deviation of log–normal distribuction
φ = reaction affinity, J
ω = rotor speed, $rad\ s^{-1}$

Literature Cited

1. Schwarzer HC, Schwertfirm F, Manhart M, Schmid HJ, Peukert W. Predictive simulation of nanoparticles precipitation based on the population balance equation. *Chem Eng Sci*. 2006;61:167–181.
2. Aoun M, Plasari E, David R, Villermaux J. Are barium sulfate kinetics sufficiently known for testing precipitation reaction models? *Chem Eng Sci*. 1996;51:2449–2458.
3. Torbacke M, Rasmuson SC. Influence of different scale of mixing in reaction crystallization. *Chem Eng Sci*. 2001;56:2459–2473.
4. Baldyga J, Pohorecki R. Turbulent micromixing in chemical reactors—a review. *Chem Eng Sci*. 1995;58:183–195.
5. Phillips R, Rohani S, Baldyga J. Micromixing in a single-feed semibatch precipitation process. *AIChE J*. 1999;45:82–92.
6. David R. General rules for prediction of the intensity of micromixing effects on precipitation. *Powder Technol*. 2001;121:2–8.
7. Bernard-Michel B, Pons M, Vivier H. Quantification, by image analysis, of effect of operational conditions on size and shape of precipitated barium sulphate. *Chem Eng J*. 2002;87:135–147.
8. Baldyga J, Orciuch W. Barium sulfate precipitation in a pipe—an experimental study and CFD modeling. *Chem Eng Sci*. 2001;56: 2435–2444.
9. Baldyga J, Orciuch W. Some hydrodynamic aspects of precipitation. *Powder Technol*. 2001;121:9–19.
10. Falk L, Schaer E. A PDF modeling of precipitation reactors. *Chem Eng Sci*. 2001;56:2445–2457.
11. Öncül AA, Sundmacher K, Thévenin D. Numerical investigation of the influence of the activity coefficient on barium sulphate crystallization. *Chem Eng Sci*. 2005;60:5395–5405.
12. Cafiero L, Baffi G, Chianese A, Jachuck R. Process intensification: precipitation of barium sulfate using a spinning disk reactor. *Indust Eng Chem Res*. 2002;41:5240–5246.
13. Barresi AA, Marchisio D, Baldi G. On the role of micro- and mesomixing in a continuous Couette-type precipitator. *Chem Eng Sci*. 1999;54:2339–2349.
14. Judat B, Kind M. Effects of mixing on precipitation of barium sulfate in a Taylor-Couette type reactor with axial flow. *Proc Int Symp Indust Crystal*. 2002;1:281–286.
15. Schwarzer HC, Peukert W. Combined experimental/numerical study on the precipitation of nanoparticles. *AIChE J*. 2004;50:3234–3247.
16. Schwarzer HC, Peukert W. Prediction of aggregation kinetics based on surface properties of nanoparticles. *Chem Eng Sci*. 2005;60:11–25.
17. Jia Z, Liu Z, He F. Synthesis of nanosized $BaSO_4$ and $CaCO_3$ particles with a membrane reactor: effects of additives on particles. *J Colloid Interface Sci*. 2003;266:322–327.
18. Wei H, Zhou W, Garside J. Computational fluid dynamics modeling of the precipitation process in a semibatch crystallizer. *Indust Eng Chem Res*. 2001;40:5255–5261.
19. Marchisio DL, Barresi AA. Simulation of turbulent precipitation in a semi-batch Taylor-Couette reactor using CFD. *AIChE J*. 2001;47:664–676.
20. Kumar S, Ramkrishna D. On the solution of population balance equations by discretization. I. A fixed point technique. *Chem Eng Sci*. 1996;51:1311–1332.
21. Marchal P, David R, Villermaux J. Crystallization and precipitation engineering. I. An efficient method for solving population balance in crystallization with agglomeration. *Chem Eng Sci*. 1988;43:59–67.
22. Muhr H, David R, Villermaux J. Crystallization and precipitation engineering. VI. Solving population balance in the case of the precipitation of silver bromide crystals with high primary nucleation rates by using first order upwind differentiation. *Chem Eng Sci*. 1996;51:309–319.
23. Marchisio DL, Pikturna JT, Fox RO, Vigil RD. Quadrature method of moments for population-balance equations. *AIChE J*. 2003;49:1266–1276.
24. King AG, Keswani ST. Colloid mills: Theory and experiment. *J Am Ceram Soc*. 1994;77:769–777.
25. Duan X, Jiao QZ. Beijing University of Chemical Technology. Chin Pat 99119385.7 (1999).
26. Zhao Y, Li F, Zhang R, Evans DG, Duan X. Preparation of layered double hydroxide nanomaterials with a uniform crystallite size using a new method involving separate nucleation and aging steps. *Chem Mater*. 2002;14:4286–4291.
27. Feng YJ, Li DQ, Li CX, Wang ZH, Evans DG, Duan X. Synthesis of Cu-containing layered double hydroxides with a narrow crystallite-size distribution. *Clays Clay Minerals*. 2003;51:566–569.
28. Shi L, Li DQ Li SF, Wang JR, Evans DG, Duan X. Preparation and characterization of Zn-Mg-Al-CO_3 LDHs flame retardants. *Flame Retardant Mater Technol*. 2005;4:21–24.
29. Lin YJ, Li DQ, Evans DG, Duan X. Modulating effect of Mg-Al-CO_3 LDHs on thermal stability of PVC resin. *Polym Degrad Stabil*. 2005;88:286–293.
30. Jiao QZ, Zhao Y, Xie H, Evans DG, Duan X. Intercalation and selective IR adsorption of hydrotalcite. *Chin J Appl Chem*. 2002;10: 96–98.
31. Vicum L, Mazzotti M, Baldyga J. Applying a thermodynamic model to the non stoichiometric precipitation of barium sulfate. *Chem Eng Technol*. 2003;26:325–333.
32. Wei H, Garside J. Application of CFD modelling to precipitation systems. *Chem Eng Res Design*. 1997;75:219–227.
33. Sefcik J, Soos M, Vaccaro A, Morbidelli M. Effects of mixing on aggregation and gelation of nanoparticles. *Chem Eng Process*. 2006; 45:936–943.
34. Randolph AD, Larson MA. *Theory of Particulate Processes*, 2nd ed. New York: Academic Press, 1988.
35. John V, Angelov I, Oncul AA, Thevenin D. Techniques for the reconstruction of a distribution from a finite number of its moments. *Chem Eng Sci*. 2007;62:2890–2904.
36. Millange F, Walton RI, O'Hare D. Time-resolved in situ X-ray diffraction study of the liquid-phase reconstructitm of Mg-Al-carboaate hydrotalcite-like compounds. *J Mater Chem*. 2000;10:1713–1720.
37. Fitchett DE, Tarbell JM. Effect of mixing on the precipitation of barium sulphate in an MSMPR reactor. *AIChE J*. 1990;36:511–522.
38. Kim W, Tarbell JM. Micromixing effects on barium sulphate precipitation in a double-jet semi batch reactor. *Chem Eng Commun*. 1999;176:89–113.
39. Chen JF, Zheng C, Chen GT. Interaction of macro- and micromixing on particle size distribution in reactive precipitation. *Chem Eng Sci*. 1996;51:1957–1966.
40. Qiang D, Nie Y, Zhang H, Gao Z. Hydrodynamic characteristics in a continuous rotor-stator mixer. I. Experimental investigation. *Chin J Process Eng*. 2007;7:1055–1059.

Manuscript received July 19, 2008, and revision received Nov. 28, 2008.